Journal of Materials Chemistry C

Accepted Manuscript

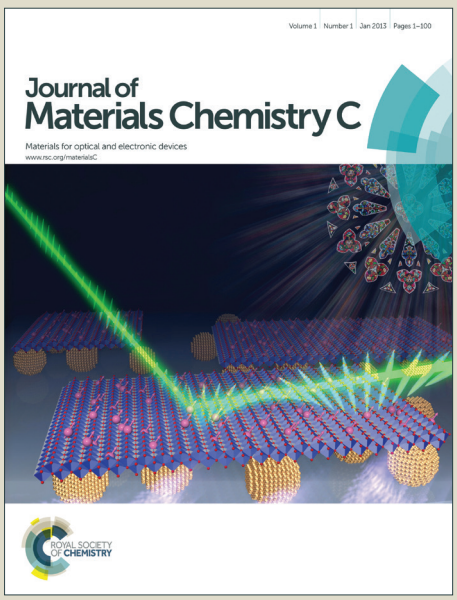

ROYAL SOCIETY OF CHEMISTRY

www.rsc.org/materialsC

Oxygen induced strained ZnO nanoparticles: An investigation of Raman scattering and visible photoluminescence

Shrikrushna Shivaji Gaikwad,[a] Ashish Chhaganlal Gandhi,[a] Swarada D. Pandit,[b] Jayashree Pant,[b] Ting-Shan Chan,[c] Chia-Liang Cheng,[a] Yuan-Ron Ma[a] and Sheng Yun Wu [*a]

[a] *Department of Physics, National Dong Hwa University, Hualien 97401, Taiwan*

[b] *Department of Physics, Abasaheb Garware College, University of Pune, India*

[c] *National Synchrotron Radiation Research Center, Hsinchu 30076, Taiwan*

[*] *Corresponding author:* sywu@mail.ndhu.edu.tw (SYWu)

Abstract

We report the influence of the nanosized effect on the optical properties of non-centrosymmetric ZnO nanoparticles. In this study confocal Raman scattering was employed to investigate the strain effect of the softening A_1(LO) phonon mode while controlling particles sizes from 55±1 to 32±1 nm. The observations reveal a positive Poisson ratio between the compressive- and tensile-strain. The intensity ratio of the A_1(2LO)/ A_1(LO) modes exhibits strong size dependence. As the particle sizes decrease further, the ratio decreases rapidly, signaling the short-range electron-phonon coupling effect which acts to confine the electrons and holes within a smaller volume. An energy red-shift in the photoluminescence peak was observed, because of a lowering in the strain of local symmetry at O^{2-} sites caused by excess oxygen, and by strong coupling between the electron and phonon vibration. The variation of the bandgap is very sensitive to the electron-phonon coupling and the distinct size effect of strained ZnO nanoparticles.

Keywords: Raman spectroscopy, ZnO, nanoparticles, strain, photoluminescence

1. Introduction

Semiconductor ZnO nanocrystals have been studied extensively over the past decade,[1-3] and results have shown a particularly efficient blue-green luminescence property that is size-dependent and hence tunable over a wide wavelength range.[4] In principle, visible-light-emission ZnO nanocrystals would be an ideal candidate as a replacement for Cd-based fluorescent labels since they are nontoxic, low cost, and chemically stable during thermal treatment in air. ZnO nanocrystals exhibit two emission bands: one for a narrow excitonic emission band in the UV range, and one for a broad band in the visible regime that has been attributed to the trap states.[5] Unlike that of the UV emission, the physical mechanism behind the visible luminescence has been very difficult to establish. What is known is that visible emission involves deep trap states arising from oxygen or zinc vacancies, electrons or holes in shallow trap states that originate from a larger surface to volume effect,[5-6] and extrinsic defects.[7] Recently, oxygen vacancies are thought to be the main cause of the visible emission as has been reported by Özgür et al.[8] Therefore, much attention has been paid in the last decades to the fabrication and structural characterization of ZnO nanostructures such as nanoparticles,[9] nanoribbons,[10] nanowires,[11] and nanorods.[12] Full exploitation of ZnO optoelectronic properties certainly requires better knowledge of the optical processes in ZnO. Shi et al.[13] reports the strong coupling of two electronic transitions strongly to lattice vibrations in ZnO which leads to an observed broad emission band with fine structure, dissipated by a phonon bath. Examining the size effect of the relation between the electron-phonon coupling and visible emission band is of great importance to understanding its physical origin. In this work, we quantified the size-dependent electron-phonon coupling and energy bandgap modulation of ZnO nanoparticles through confocal Raman scattering and

photoluminescence, respectively. Here, as grown ZnO nanoparticles were synthesized using the microwave reaction. The size of the nanoparticles was controlled by tuning the annealing temperature. Energy dispersive spectroscopy (EDS) was successfully utilized to quantitatively estimate the differences in atomic percent of zinc and oxygen in as-synthesized ZnO nanoparticles. An energy red-shift in the photoluminescence peak was observed, because of a lowering in the strain of local symmetry at O^{2-} sites caused by excess oxygen, and by strong coupling between the electron and phonon vibration, as noted using Raman spectroscopy. This will be discussed below.

2. Experimental details

ZnO nanoparticles were synthesized using the method developed by Spanhel and Anderson,[14] with a few modifications described earlier.[15] Briefly, aqueous solutions of Zinc Acetate and Sodium Hydroxide were used with a molar ratio of 1:2. These were mixed together and stirred for 15 minutes. Triethylamine was added to the above mixture and stirring continuously until a uniform thick milky white slurry was obtained. All the chemicals were obtained from Merck and used as received. The mixture was heated in a Raga scientific microwave system for 15 minutes at 280 W. It was then centrifuged at 2000 rpm for two minutes. The residue was washed with distilled water and then with ethanol. It was then dried overnight in air. The as-prepared sample was calcined at 400 ℃ for 2 hours. The as-grown sample was then placed in a ceramic boat inside a quartz tube. The tube was evacuated to about 10^{-3} Torr using a mechanical pump and heated in a tube furnace at various temperatures ranging from 500 to 800 ℃ for 2 hours. Size and morphological analysis was carried out using field-emission scanning electron microscopy (SEM) with a JEOL JSM-6500F, JEOL Ltd. microscope from Japan. The energy dispersive

spectroscopy (EDS) technique was used to estimate to atomic percentage of zinc and oxygen in each ZnO nanoparticle. Analysis of the crystalline properties was carried out using synchrotron x-ray diffraction (XRD). Samples prepared at various annealing temperatures were mounted in a rotor sample holder for examination by a synchrotron x-ray diffractometer. Synchrotron x-ray diffraction patterns were obtained using a large Debye-Scherrer camera installed on the BL01C2 beam line instrument at the National Synchrotron Radiation Research Center in Taiwan, with an incident wavelength of λ = 0.7749 Å. A high energy synchrotron radiation XRD technique should be employed for detailed investigation of the strain leading to the annealing effect of ZnO nanoparticles, because small changes in strain are undetectable with the usual XRD techniques. The phonon and photoluminescence properties of ZnO nanoparticles were investigated using a Confocal Raman spectrometer (Alpha 300, WiTec Pte. Ltd., from Germany) equipped with a piezo scanner and 9100 microscope objective lens (n.a. = 0.90; Nikon Imaging Japan Inc., Japan). The samples were excited with a 488-nm Ar ion laser (CVI Melles Griot, Carlsbad, USA) (0.05 mW laser power), to form a spot 0.3 μm in diameter, giving a power density of 100 mW cm^{-2}.

3. Results and discussion

3.1 Morphological analysis

We first investigate the evolution of the morphologies of ZnO nanoparticles at various annealing temperatures T_A. The SEM images of the ZnO nanoparticles are shown in Figure 1a-f. No particular morphological change was observed at a low annealing temperature (T_A=400℃) (see Figure 1a). The interconnecting nanoparticles are stuck together in clusters due to electrostatic effects as well as an artifact of the drying of aqueous suspensions. Further annealing at 500, 600, 700 and 800℃ resulted

in the dehydration of the precipitate and the formation of well separated and uniformly distributed spherical nanoparticles, as can be seen from Figure 1b-d. However samples annealed at 700 and 800 ℃ (see Figure 1e-f) showed a tendency towards agglomeration. An evaluation of the diameter distribution can be obtained and calculated from a portion of the SEM images, as shown in Figure 1g. The distributions of the diameters were quite asymmetric and could be described using a log-normal distribution function. The solid curves represent the fit assuming a log-normal distribution function. The log-normal distribution function is defined as follows: $f(d)=\frac{1}{\sqrt{2\pi}d\sigma}\exp\left(-\frac{(\ln d-\ln<d_{SEM}>)^2}{2\sigma^2}\right)$, where $<d_{SEM}>$ is the mean diameter and σ is the standard deviation of the function. The mean diameters $<d_{SEM}>$ of ZnO nanoparticles synthesized and annealed at 400, 500, 600, 700, and 800 ℃, as determined from the SEM images and described by the fit to the log-normal function, are approximately 44±2, 60±2, 74±7, 115±14 and 138±18 nm, respectively. The corresponding fitting parameters are listed in Table 1. The obtained value of the standard deviation of the fitted function is less than 0.4 for all ZnO nanoparticles, showing that the distribution was confined to a limited range. And the mean size $<d_{SEM}>$ of the ZnO nanoparticles was found to be dependent on the annealing temperature and time. The T_A dependence of the mean sizes were obtained and calculated from a portion of the SEM image, as shown in Figure 2, where the solid curve shows the fit to the growth law. This can be well described as follows: $<d_{SEM}>=64-0.2T_A+0.00037T_A^2$. In this present study, the growth temperature of ZnO nanoparticles was confined to between 400 to 800 ℃, which is 0.202 and 0.405 times the melting point of ZnO (1975 ℃), following Wagner's scaling theory.[16] This result differs from the previous report from Goswami's group[17] who concluded that a higher annealing temperature (~ 600 ℃) assists in obtaining pure ZnO nanoparticles without

affecting their size and crystal structure. They used a chemical precipitation technique. In this method, the growth of nanoparticles is controlled by their pH concentration. The annealing of nanoparticles assists in removing carbonate impurities and moisture so as to obtain pure ZnO nanocrystals. At a higher annealing temperature region (~900 ℃), as shown in the inset to Figure 2, it can be seen that the morphologies of the samples are different from the others (400-800 ℃) and large grains are generally present on the surface of the sample. This indicates that the nanoparticles can be melted at about 900 ℃, which is much lower than the melting point of bulk ZnO. Similar results have been reported in a ZnO nanorod system,[18-19] in which ZnO nanorods melted and changed into particles at 950 ℃ and 900 ℃. Moreover, theoretical investigation has also demonstrated that the melting temperature will decrease with the reduction of the sizes of nanostructures.[20] In order to further understand the effect of annealing on the properties of ZnO nanoparticles, we characterize the oxygen concentration in ZnO nanoparticles after annealing treatment, finding the evolution in the ratio of oxygen and zinc with an increase in both annealing temperature and particle size.

3.2 Stoichiometric analysis

The ZnO nanoparticles, as synthesized through chemical means show an evolution of particle size with an increase of the annealing temperature from 400 to 800 ℃, as is also observed in SEM images. Depending on the fabrication conditions, native defects (such as oxygen vacancies, interstitials, and antisites) or extrinsic defects can be introduced, thus leading to the control of the phonons, electronic structure, and the luminescence response in the visible regime of the ZnO nanoparticles. Energy dispersive spectroscopy (EDS) is a useful technique for estimation of the atomic percent of constituent elements in a given sample. Figure 3a

shows the EDS results (Inca x-sight model 7557, Oxford Instruments, UK), from which it can be seen that the elemental spectra of different nanoparticles are associated with a series of elemental zinc and oxygen constituents which can be assigned to Zn-Lα_1, Zn-Kα_1, and O-Kα_1. The estimated atomic percent ratio of oxygen/zinc (obtained using EDS) with respect to the annealing temperature is plotted in Figure 3b. The figure shows an increase in the oxygen/zinc atomic percent with increasing annealing temperature (i.e., increasing nanoparticle size). The increase in the ratio of O/Zn (less than 1) in the range of 400 to 500 ℃ reveals that it is likely that the formation proceeds through the nucleation of oxygen deficient ZnO_{1-x} during the lower annealing temperature, which is in agreement with previous results.[21-22] In their comprehensive results, it was observed that the modification of the surface with hydrogen peroxide could significantly reduce the persistent photoconductivity relaxation time, implying that a deficiency of surface oxygen was responsible for the effect. The oxygen deficiency was further reduced after increasing the thermal treatment, leading to a sharp increase in the ratio of oxygen/zinc from 0.95 to 1.12. These observations indicate that the thermal treatment alters the surface stoichiometry resulting in a conversion from a state of oxygen deficiency to that of excess oxygen.

3.3 Analysis of X-ray diffraction

The presence of lattice strain is a common phenomenon in the majority of multilayer thin films and heterostructures, and can influence the physical properties of these structures significantly.[23-24] X-ray diffraction analysis is widely used to determine the lattice strain in nanostructures and sensitive to very small changes of lattice parameters. The high energy synchrotron radiation X-ray diffraction (SR-XRD) technique must be employed for detailed investigation of the crystalline structure of

ZnO nanoparticles, because small changes in strain are undetectable by commercial x-ray diffractometer. Figure 4 displays the dependency on annealing temperature T_A in the x-ray diffraction patterns. Here, different colors are used to indicate the peak intensity of the diffraction patterns. At the bottom of Figure 4, three significant broader nuclear peaks at the (1 0 0), (0 0 2), and (1 0 1) positions are visible, indexed based on the space group of $P6_3mc$. With an increase of annealing temperature, there is a decrease in the full width at half-maximum (FWHM) and corresponding increase in the particle size. The observed broadening of the peak is a short range behavior, which can be described by the Gaussian instrument resolution function, as discussed in our previous report.[25] As can be seen in Table 2, the FWHM shows a rapid decrease in the peak profile of (1 0 0) from 0.0421±0.0001 to 0.0193±0.0001 rad. as the T_A increases from 400 to 800 ℃, signaling the development of crystallinity from short- to long-range ordering. The full width at half-maximum of peak β and ZnO nanoparticle sizes $<d_{XRD}>$ were estimated using the Williamson-Hall method[26] and the Scherrer formula[27] $\beta = \frac{1}{\cos\theta}\left(\frac{094\lambda}{< d_{XRD} >} + 4\eta\sin\theta\right)$, where λ is the incident wavelength of X-ray, θ is the diffraction angle and η is the local lattice distortion parameter. Figure 5 displays the plot of $\beta\cos\theta/094\lambda$ vs. $4\sin\theta/094\lambda$ for all samples. The ZnO nanoparticles size $<d_{XRD}>$ and the local lattice distortion η can be estimated by fitting and extrapolating the linear curve to the zero value of the x-axis, respectively. The slope of the linear curve gives the value of the local lattice distortion η; the obtained values of lattice distortion for different ZnO nanoparticles are in the range of 0.146 to 0.022 %. These values of lattice distortion are in good agreement with those previously reported for ZnO nanoparticles.[28-29]

The interception of the fitted linear curve to the y-axis gives the inverse crystalline size. The observed crystalline sizes $<d_{XRD}>$ for ZnO nanoparticles

synthesized by annealing at 400, 500, 600, 700, and 800 °C are 32±1, 38±2, 44±3, 51±2, and 55±1 nm, respectively. The obtained crystalline sizes are smaller than the mean nanoparticle diameters obtained from the SEM images. The observed discrepancy is due to the agglomeration behavior of the nanoparticles, resulting in the formation of a crystalline domain inside each nanoparticle. As discussed in the introduction, Raman spectroscopy is dependent on the long range crystalline order, therefore from here onwards we will use the crystalline size obtained from the Williamson-Hall plot as the nanoparticle size rather than the particle size obtained from SEM images.

The X-ray diffraction patterns of the ZnO nanoparticles are further refined using Rietveld analysis.[30] The diffraction pattern (black crosses) taken at various annealing temperatures T_A are shown, and the solid curve (red curve) indicates the fitted pattern. The difference (blue curve) between the observed and the fitted pattern is plotted at the bottom of Figure 6a-e. The obtained refined lattice parameters confirm the formation of wurtzite (*hcp*) ZnO having a space group of $P6_3mc$ (as tabulated in Table 2). The wurtzite structure has a hexagonal unit cell with two lattice parameters, a and c with a ratio of c/a=1.633. In a real ZnO crystal, the wurtzite structure deviates from the ideal arrangement, by changing the c/a ratio and the u parameter (which is a measure of the amount by which each atom is displaced with respect to the next along the c-axis). Bond length along the c-axis is longer than the other three bonds because the ZnO_4 tetrahedra are distorted along the c-axis, which results in a dipole moment. The polarity is responsible for a number of the properties of ZnO, including its piezoelectricity and spontaneous polarization, and is also a key factor in crystal growth and defect generation. In general, the axial ratio of c/a and u parameter can be used as a common indicator for the polarity as the deviation occurs in the lattice of ZnO crystal. Figure 6f shows the relation between the mean sizes and

the ratio of $R=c/a$, revealing a strong long-range polar interaction when the c/a ratio decreases. The inset to Figure 6f shows a noncentrosymmetric polar structure that is made up of alternate layers of positive and negative ions, leading to spontaneous polarization. The solid curve in Figure 6f describes an exponential decay function, namely $R = R_o + \beta e^{-\frac{<d_{XRD}>}{\zeta_o}}$, where β=0.0013±0.0001, ξ_o= 63±3 nm, and R_o=1.601±0.002 represent the fitted parameters, the domain size and ratio of long range polar interaction, respectively. Furthermore, this result shows a rapid decrease as size increases, signaling the development of short to long range polar interaction. As discussed above, our experimental results indicate that the ratio of c/a plays an important role in ZnO nanoparticle polarity. The obtained domain size is closer to the theoretical predication, as reported by Herng et al.[31] and the experimental grain size (~ 50 nm) of ZnO prepared at a temperature range of 200-400 ℃. The formation ability of short range polarization interactions of the domain wall with grain size is also estimated based on first principle calculation. It is found that domain wall can occur spontaneously at room temperature if the grain size is larger than 25 nm,[32] resulting in an increasing of c/a ratio as size decreases. It is worth noting that the nucleation of domain walls from the short- to long- range polarization interaction is close to those obtained in our present study, with ZnO particle sizes ranging from 32±1 to 55±1 nm. This observation implies that the higher c/a ratio in smaller ZnO nanoparticles could originate from a spontaneous charge carrier separation induced by intrinsic surface strain as has been reported by Kuo et al. using the first-principles calculation.[29] In this work, they found that the shrinking strain induced by surface reconstruction causes the electrons and holes to separate and move toward the core and surface region, respectively. It can be further assumed that, in addition, a net strain-induced positive charge on the surface of ZnO nanoparticles could influence

the band gap shift and electron-phonon coupling, as has been reported by Wei et Al.[33] In this case, the Raman and photoluminescence experiments could provide a considerable amount of valuable information for clarifying this issue.

3.4 Electron-phonon study of ZnO nanoparticles

Analyzing possible electron-phonon coupling and strain in ZnO is especially interesting because of its increasing technological applications in optoelectronic devices.[34] In this study, it is of great interest to directly observe the effect of ZnO nanoparticle size and polarization induced strain arising from phonon vibration. Here we used confocal Raman spectroscopy to analyze the strain state of the ZnO nanoparticles since it has the high spatial resolution and sensitivity necessary for probing the local atomic vibration and lattice deformations. ZnO has a wurtzite structure with C_{6v} symmetry, and is characterized by two interconnecting sublattices of Zn^{2+} and O^{2-}, such that each Zn ion is surrounded by tetrahedra of O ions, and vice-versa. This tetrahedral coordination gives rise to polar symmetry along the hexagonal axis. The four face terminations of wurtzite ZnO are the polar Zn terminated (0001) (*c*-axis) and O terminated $(000\bar{1})$ faces, and the non-polar $(11\bar{2}0)$ (*a*-axis) and $(10\bar{1}0)$ faces which both contain an equal number of Zn and O atoms. Group theory predicts the Raman active zone-centers of the optical phonons with the symmetry: A_1, E_1, and E_2 mode.[35] The phonons having A_1 and E_1 symmetry are polar phonons and, hence, the transverse-optical (TA) and longitudinal-optical (LO) phonons exhibit different frequencies. Nonpolar phonon modes with symmetry E_2 have two frequencies: E_{2H}(high) is associated with oxygen atoms and E_{2L}(low) is associated with the Zn sublattice. All described phonon modes have been reported in the Raman-scattering spectra of bulk ZnO.[36] Figure 7a shows a series of Raman spectra taken at room temperature from ZnO nanoparticles synthesized by annealing

at 400, 500, 600, 700, and 800 ℃. The anomalous behaviors can be analyzed quantitatively using the profile fitting method. These peaks, including the phonon and two magnon modes, were analyzed using the Voigt function covering the whole regime. The solid line in Figure 7a represents the fitting line using the Voigt function. The detailed annealing temperature T_A and the particle size dependencies of the peak position and FWHM are listed in Table 3. Based on the reported zone-center optical phonon frequencies in ZnO, one can assign the Raman peak at 330±0.7 cm^{-1} to E_{2H}-E_{2L}, the peak at 437.5±0.2 cm^{-1} to E_{2H}, the peak at 583.1±0.7 cm^{-1} to A_1(LO) and the peak at 685.5±6.9 cm^{-1} to the TA+LO mode. In addition to the conventional LO phonon mode, we observe a lower intensity at 536 cm^{-1} which has been attributed to surface phonon. Furthermore, the surface phonon may not be observable in our smaller nanoparticles, due to both lower resonant conditions and weaker surface electron-phonon coupling.[37] When the size is reduced to the nano scale, the phonon scattering will not be limited to the center of the Brillouin zone, and the phonon dispersion near the zone center must also be considered. As a result, a shift of the first order optical phonon can be observed. Figure 7b shows the size effect of the integrated intensity of first order Raman scattering of the A_1(LO) phonon mode. A clear decrease in intensity and blue shift of the peak can be seen with decreasing particle size. The observed results are in good agreement with those of Gomi et al.,[38] who argued that Zn and oxygen are stacked alternately along the *c*-axis. Any lattice irregularity such as oxygen defects would affect the displacement of ions in the A_1 mode more than in the E_1 mode, reflecting a decrease in the intensity of the A_1 mode. However, an intrinsic problem for oxygen deficiencies of various sizes can also be examined using photoluminescence study, as will be discussed later. Next, we will evaluate the ratio between the second- and first-order Raman scattering cross-sections of various particle sizes, extracting information about the electron-phonon (*e-ph*)

coupling. CdS, CdSe,[39] InP,[40] and ZnO[36] nanocrystals have been intensively studied by this method. The ratio was found to be associated with the dimensionless displacement Δ for the Frohlich interaction in a solid[41] given by

$$\Delta = 1.97 \frac{e^2}{a_o h \omega_{LO}} \left(\frac{1}{\varepsilon_\infty} - \frac{1}{\varepsilon_o}\right) \frac{1}{\omega} \int_{x=0}^{\omega} x^4 (2 + x^2)^2 (1 + x^2)^{-4} dx ,$$

where a_o is the lattice constant, $\omega = (3\pi^2)^{1/3} \frac{a_o}{a_b}$, a_b is the exciton Bohr radius, and ε_o and ε_∞ are low and high frequency dielectric constants, respectively. Figure 7c shows the particle size dependence of the intensity ratio of A_1(2LO) and A_1(LO) mode; the dashed line represents the calculated value of Δ = 2.85 for bulk ZnO. The intensity ratio of these modes exhibits strong size dependence. As the particle size decreased further, the intensity ratio of the A_1(2LO) and A_1(LO) mode rapidly decreased, signaling the finite size effect, which acts to confine the electron and hole into a smaller volume. In addition the Frohlich coupling strength could diminish, because the electric field caused by the vibration should be less effective in polarizing the excitons.[42] These characteristics are in agreement with previously reported results for ZnO nanowires.[37] In one comprehensive analysis, the ratio was found to increase with increasing nanowire diameter. It was concluded that the quantum confinement strongly modifies the eigenfunctions in nanocrystals, causing the change of magnitude of the electron-phonon coupling strength.

3.5 Anisotropic strain study of ZnO nanoparticles

To obtain a clear picture of the relation between strain and phonon vibration along the *c*-axis, we were only able to analyze spectra corresponding to the A_1(LO) phonon mode. In previous studies, the size induced shift of the A_1(LO) phonon has been discussed by the Demangeot group[43] in ZnO nanoparticles and Alim *et al* [44] in ZnO nanocrystals. They observed a shift of the phonon frequency of up to 8 cm^{-1}

achieved by increasing the size of the nanoparticles from 3.2 to 8 nm. The origin of this frequency shift is still unclear except for local heating effects. The shift of A_1(LO) phonon frequency contains information about the strain, LO-plasmon coupling, and polar phonons that are sensitive to the interactions with free carriers. The strain induced frequency up-shift of the A_1(LO) phonon mode is given by

$$\Delta \omega_{A1} = a(\varepsilon_{xx} + \varepsilon_{yy}) + b\varepsilon_{zz},$$

where *a* and *b* are the deformation potential constants. Experimental values reported by Callsen et al.[45] for the A1(LO) mode in ZnO are *a*=-577 cm^{-1} and *b*=-599 cm^{-1}. In the present study, we assume that the in-plane strain is biaxially isotropic, $\varepsilon_{xx}=\varepsilon_{yy}$, and the in-plane strain ε_{xx} and the out-of-plane strain ε_{zz} are related by

$$\varepsilon_{zz} = -\frac{2C_{13}}{C_{33}}\varepsilon_{xx},$$

where C_{13} and C_{33} are the elastic constants of ZnO with C_{13}=104.8 GPa and C_{33}=206.9 GPa, as reported by Shein et al.[46] Figure 8a-b displays the size effects of the calculated in-plane ε_{xx} and out-of-plane ε_{zz}, reflecting the existence of tensile- and compressive-strain, respectively. With decreasing particle size, the surface layer is compressively strained along the *c*-axis and as a consequence is under tensile strain in the perpendicular direction. The Poisson effect induces an out-of-plane strain of the opposite sign. This result is in agreement with the prediction of a theoretical simulation of pristine ZnO nanowires by Kou et al.[24] In their comprehensive calculation, they stated that the surface intrinsic strain induces a charge carrier separation. As compressive strain is increased, the band-edge states tend to delocalize in comparison with the zero strain case, since the axial compression must lead to the elongation of the out-of-plane surface bond length due to a positive Poisson ration ($\upsilon=-\varepsilon_{xx}/\varepsilon_{zz}$). We further characterize and quantify the dependence of the size on the compressive- and tensile-strain. This can be roughly expressed as

$\varepsilon = \varepsilon^{o} + Ae^{-\frac{<d_{XRD}>}{d_o}}$, where ε^{o} is the initial strain at a large size and d_o is the critical size. A significant critical size of d_o ~ 68±5 nm was found from the fitting, indicating that the size effects on strain could result in a tendency for band offset between strained and unstrained regions of ZnO nanoparticles. As a result, the energies of the edge-states demonstrate an opposite change tendency in response to the strain: the energy of the valence band (conduction band) state is shifted upwards (downwards) by tensile strain and downwards (upwards) by compressive strain. The influence of a narrow (broad) band gap can be investigated through photoluminescence (PL) spectroscopy.

3.6 Size effect of photoluminescence

PL measurement is a helpful technique to explore the optical properties of semiconducting nanoparticles. It informs us about the energy states of impurities and defects, even at very low densities, which is helpful in understanding structural defects, the crystallinity, surface defects, energy bands and find exciton structures. Defects like oxygen vacancies at the grain boundaries and the presence of doping atoms in the surface and inter-granular layers can affect some physical properties (such as the optical properties) of nano-grained metal oxide materials.[47] Moreover, the shifts in the bandgap of strained nanocrystals, including uniaxial compressive- and tensile-strains, have been widely investigated through theoretical calculations.[48-49] However, there have been few reports[23, 33] relating experimental confirmation of systematic investigations of this phenomenon.

The ZnO nanoparticles were excited by a 488 nm wavelength laser at room temperature. The broad peaks in spectra at various sizes were de-convoluted using two Gaussian distributions (illustrated by solid curves). The corresponding fitting

parameters are presented in Table 4. A prominent peak was obtained in the spectra, with the main peak at 569.6±0.4 nm (~2.21 eV) exhibiting strong mid-gap green emission with $<d_{XRD}>$=32±1 nm, as shown in Figure 9a. This peak position is close to the results previously reported by Rakshit et al.[50] in ZnO:MgO nanocrystals. They reported the presence of two distinct defects (~ 520 and 570 nm, respectively). The feature at 570 nm had been interpreted to originate from the recombination of photo generated holes trapped in shallow states that lie close to the valence band with the deep trap states. With decreased particle size, a significant energy red-shift band at 725.7±1.6 nm (~ 1.71 eV with $<d_{XRD}>$=55±1 nm, shown in Figure 9b) spanning the entire visible range and quenching the mid-gap green emission at larger size provides further evidence of lower oxygen deficiency in the ZnO nanoparticles.[51] The variation of the bandgap is very sensitive to the electron-phonon coupling and the distinct size effect of strained ZnO nanoparticles. The origin of these emissions, especially the green emission, has been controversial. A number of previous reports have attributed it to Zn interstitials[52] and Zn vacancies.[53] The most widely accepted origin of the green emission is typically associated with oxygen deficiency; orange emission is associated with excess oxygen.[54-55] This is in excellent agreement with the experimental EDS results. It should be noted that the broad visible emission band contains at least two contributions, originating from surface-defect-related states, such as the recombination of deep trap electrons with free VB holes or holes in shallow traps, as shown in Figure 9c. The recombination of an electron-hole pair can exist as a Wannier exciton and when it recombines radiatively, a photon creates energy close to the visible regime in the ZnO nanoparticles. The electron/hole from a Wannier exciton can be trapped in the particle. This can take place in shallow levels or in deep traps. As the band edges shift as a function of particle size,[56] the energetic position of a shallow trap shows a similar size dependence. As observed in Figure 9a,

and also previously reported by several groups,[57-58] there is broad visible emission of oxygen deficiency/excess induced red-shifts with increasing nanoparticle size. This suggests that the defect states are associated with the deep-(electron) and shallow-(hole) trap of the nanoparticles and follows analogous energetic shifts with the degree of excitonic confinement. Shi et al.[13] and Beane et al.[59] reported that the visible emission from zinc oxide particles is broader than can be fitted using the Huang-Rhys model to describe the coupling of an electronic state with a vibration state. This suggests that the strong coupling of the electronic transition to the lattice vibrations of ZnO is responsible for the broad visible emission band. Recent study of single ZnO nanoparticles by Layek et al.[60] demonstrates that the broad emission originates from the coupling of excited states and phonon modes rather than polydipersity. As discussed above, our Raman and PL experimental results indicate that particle size plays an important role in the optical properties of ZnO.

4. Conclusion

In conclusion, we demonstrated the potential of synchrotron X-ray diffraction and confocal Raman spectroscopy for studying the nanosized, strain, and electron-phonon coupling in ZnO nanoparticles through investigation of the phonon excitation and photoluminescence. EDS observations indicate that the thermal treatment alters the surface stoichiometry resulting in a conversion from a state of oxygen deficiency to that of excess oxygen. The observed *c/a* lattice ratio shows a rapid decrease with increasing size, signaling the development of short to long range polar interaction, which has been attributed to the size effect. The value obtained for the intensity ratio of $A_1(2LO)/ A_1(LO)$ modes can be used to calculate the strength of the electron-phonon coupling coefficient Δ that is responsible for the broad visible emission bands. A weakened electron-phonon coupling was observed as strain and

corresponding bandgap variation were decreased by increasing the size of strained ZnO nanoparticles. These results reveal that the electron-phonon coupling, strain, and oxygen concentration within the nanoparticles dominate the shift of visible emission, whereas the dependence of the visible emission band energy on the particle size implies that a delocalized charge carrier is involved in the emission process.

Author contact information

*Correspondence and requests for material should be addressed by e-mail to: sywu@mail.ndhu.edu.tw (SYWu).

Authors' contributions

SYW wrote, conceived, and designed the experiments. SSG, SDP, and JP grew the samples. SSG and ACG collected and analyzed the data. TSC, CLC, and YRM contributed the experimental facilities for the x-ray, confocal Raman, and SEM measurements, as well as valuable discussions. All the authors discussed the results, contributed to the text of the manuscript, commented on the manuscript, and approved its final version.

Competing interests

The authors declare that they have no competing financial interests.

Acknowledgements

We would like to thank the National Science Council of the Republic of China for their financial support through project number NSC-100-2112-M-259-003-MY3 (SYWu). We would also like to thank the Indian Space Research Organization, and University of Pune for their financial support through project number GOI-A-337(B) (111) (JPant).

References

1 S. Sadhu, M. A. Tachiya, *J. Phys. Chem.* 2009, **113**, 19488–19492.

2 A. R. Clapp, I. L. Medintz, J. M. Mauro, B. R. Fisher, M. G. Bawendi, H. Mattoussi, *J. Am. Chem. Soc.* 2004, **126**, 301– 310.

3 A. M. Funston, J. J. Jasieniak, P. Mulvaney, *Adv. Mater.* 2008, **20**, 4274–4280.

4 M. Jr. Bruchez, M. Moronne, P. Gin, S. Weiss, P. A. Alivisatos, *Science* 1998, **281**, 2013-2016.

5 K. Vanheusden, W. L. Warren, C. H. Seager, D. R. Tallant, J. A. Voigt, B. E. Gnade, *J. Appl. Phys.* 1996, **79**, 7983-7990.

6 S. A. Studenikin and M. Cocivera, *J. Appl. Phys.* 2002, **91**, 5060-5065.

7 H. Wei, Y. Wu, L. Wu, C. Hu, *Mater. Lett.* 2005, **59**, 271-275.

8 U. Özgür; Ya, I. Alivov; C. Liu; A. Teke; M. A. Reshchikov; S. Doğan; V. Avrutin, S. –J. Cho; H. Morkoç, H. *J. Appl. Phys.* 2005, **98**, 041301.

9 Y. Wang, F. Zhao, P. Xie, S. Liang, S. Deng, N. Xu, Opt. Commun. 2007, **276**, 186-190.

10 A. B. Djurisic, W. C. H. Choi, V. A. L. Roy, Y. H. Leung, C. Y. Kwong, K. W. Cheah, G. T. K. Rao, W. K. Chan, H. F. Liu, C. Surya, *Adv. Func. Mater.* 2004, **14**, 856-864.

11 P. –H. Shih, H. –J. Hung, Y. –R. Ma, S. Y. Wu, *Nanoscale Res. Lett.* 2012, **7**, 354.

12 D. W. Bahnemann, C. Kormann, M. R. Hoffmann, *J. Phys. Chem.* 1987, **91**, 3789-3798.

13 S. L. Shi, G. Q. Li, S. J. Xu, Y. Zhao, G. H. Chen, *J. Phys. Chem. B* 2006, **110**, 10475-10478.

14 L. Spanhel, M. A. Anderson, *J. Am. Chem. Soc*. 1991, ***113***, 2826-2833.

15 E. A. Meulenkamp, *J. Phys. Chem*. B 1998, ***102***, 5566-5572.

16 C. Wagner, *Z. Phys. Chem. B* 1933, **21**, 25.

17 Navendu Goswami, Dhirendra Kumar Sharma, *Physica E* 2010, **42**, 1675-1682.

18 Y. –F. Tu, Q. –M. Fu, J. –P. Sang, Z. –J. Tan, Z. –W. Zou, *Mater. Lett.* 2012, **86**, 80-83.

19 Z. Yan, Y. Ma, D. Wang, J. Wang, Z. Gao, L. Wang, P. Yu, T. Song, *Appl. Phys. Lett.* 2008, **92**, 081911.

20 G. Guisbiers, S. Pereira, *Nanotechnology* 2007, **18,** 435710.

21 Z. G. Yin, X. W. Zhang, Z. Fu, Z. L. Yang, J. L. Wu, G. S. Wu, L. Gong, Paul K. Chu, *Phys. Status. Solid RRL* 2012, **6**, 117-119.

22 Q. L. Gu, C. C. Ling, X. D. Chen, C. L. Cheng, A. M. C. Ng, C. D. Beling, S. Fung, A. B. Djurišić, L. W. Lu, G. Brauer, H. C. Ong, *Appl. Phys. Lett.* 2007, **90**, 122101.

23 S. Y. Yang, D. Prendergast, J. B. Neaton, *Nano Lett.* 2010, **10**, 3156-3162.

24 Qiong Gao, Jing Wen, Xin Liu, Lili Wu, Hong Gao, Xitan Zhang, *J. Phys. Chem. C* 2013, **117**, 14247-14253.

25 S. Y. Wu, J. –Y. Ji, M. H. Chou, W. –H. Li, G. C. Chi, *Appl. Phys. Lett.* 2008, **92**, 161901

26 G. K. Williamson, W. H. Hall, *Acta Metall.* 1953, **1**, 22-31

27 B. E. Warren, X-ray Diffraction. Addsion-Wesley, Reading, MA, 1969

28 Jiaqiang Xu, Qingyi Pan, Yu'an Shun, Zhizhuang Tian, *Small* 2000, **66**, 277-279.

29 Liangzhi Kuo, Chun Li, Zi-Yue Zhang, Changfeng Chen, Wanlin Guo, *Appl. Phys. Lett.* 2010, **97**, 053104.

30 H. M. Rietveld, *J. Appl. Cryst.* 1969, ***2***, 65–71.

31 T. S. Herng, A. Kumar, C. S. Ong, Y. P. Feng, Y. H. Lu, K. Y. Zeng, J. Ding, *Sci. Rep.* 2012, **2**, 587.

32 A. D. Corso, M. Posternak, R. Resta, A. Baldereschi, *Phys Rev* B 1994, **50**,

10715.

33 Bin Wei, Kun Zheng, Yuan Ji, Yufei Zhang, Ze Zhang, Xiaodong Han, *Nano. Lett.* 2012, **12**, 4595-4599.

34 C. F. Klingshirn, A. Waag, A. Hoffmann, J. Geurts, Zinc Oxide: From Fundamental Properties towards Novel Applications. Springer, Berlin, 2010.

35 R. Loudon, *Adv. Phys.* 1964, **13**, 423-482.

36 N. Ashkenov, B. N. Mbenkum, C. Bundesmann, V. Riede, M. Lorenz, D. Spemann, E. M. Kaidashev, A. Kasic, M. Schubert, M. Grundmann, G. Wagner, H. Neumann, H. Arwin, B. Monemar, *J. Appl. Phys.* 2003, **93**, 126-133.

37 R. P. Wang, G. Xu, P. Jin, *Phys. Rev. B* 2004, **69**, 113303.

38 M. Gomi, N. Oohira, K. Ozaki, M. Koyano, *Jpn. J. Appl. Phys.* 2003, **42**, 481.

39 A. P. Alivisatos, T. D. Harris, P. J. Carroll, M. L. Steigerwald, L. E. Brus, *J. Chem. Phys.* 1989, **90**, 3463-3468.

40 J. J. Shiang, R. H. Wolters, J. R. Health, *J. Chem. Phys.* 1997, **106**, 8981-8987.

41 R. Merlin, G. Guntherodt, R. Humphreys, M. Cardona, R. Suryanarayanan, F. Hoizberg, *Phys. Rev. B* 1978, **17**, 4951-4958.

42 S. Schmitt-Rink, D. A. B. Miller, D. S. Chemla, *Phys. Rev. B* 1987, **35**, 8113-8125.

43 F. Demangeot, V. Paillard, P. M. Chassaing, C. Pagès, M. L. Kahn, A. Maisonnat, B. Chaudret, *Appl. Phys. Lett.* 2006, **88**, 071921.

44 K. A. Alim, V. A. Fonoberov, M. Shamsa, A. A. Balandin, *J, Appl. Phys.* 2005, **97**, 124313.

45 G. Callsen, J. S. Reparaz, M. R. Wanger, R. Kisdte, C. Nenstile, A. Hoffmann, M. R. Phillips, *Appl. Phys. Lett.* 2011, **98**, 061906.

46 I. R. Shein, V. S. Kiîko, Yu N. Makurin, M. A. Gorbunova, A. L. Ivanovskiî, *Phys. Solid State* 2007, **49**, 1067-1073.

47 Y. G. Wang, S. P. Lau, H. W. Lee, S. F. Yu, B. K. Tay, X. H. Zhang, H. H. Hng, *J. Appl. Phys.* 2003, **94**, 354-358.

48 Y. R. Yang, X. H. Yan, Y. Xiao, D. Lu, *Appl. Phys. Lett.* 2010, **97**, 033106.

49 S. Li, Q. Jiang, G. W. Yang, *Appl. Phys. Lett.* 2010, **96**, 213101.

50 S. Rakshit, S. Vasudevan, *J. Phys. Chem. C* 2009, **113**, 16424-16431.

51 M. Ghosh, A. K. Raychaudhuri, *Nanotechnology* 2008, **19**, 447504.

52 L. K. Korsunska, L. V. Borkovska, B. M. Bulakh, L. Yu Khomenkova, V. I. Kushnirenko, I. V. Markevichthe, *J. Lumin.* 2003, **102-103**, 733-736.

53 A. F. Kohan, G. Ceder, D. Morgan, C. G. Van de Walle, *Phys. Rev. B* 2000, **61**, 15019-15027.

54 N. E. Hsu, W. K. Hung, Y. F. Chena, *J. Appl. Phys.* 2004, **96**, 4671-4673.

55 A. Studenikin, N. Golego, M. Cocivera, *J. Appl. Phys.* 1998, **84**, 2287.

56 D. W. Bahnemann, C. Kormann, M. R. Hoffmann, *J. Phys. Chem.* 1987, **91**, 3789-3798.

57 S. Chakrabarti, D. Ganguli, S. Chaudhuri, *Phys. Status Solidi A* 2004, **201**, 2134– 2142.

58 A. Wood, M. Giersig, M. Hilgendorff, A. Vilas-Campos, L. M. Liz-Marzan, P. Mulvaney, *Aust. J. Chem.* 2003, **56**, 1051– 1058.

59 G. A. Beane, A. J. Morfa, A. M. Funston, P. Mulvaney, *J. Phys. Chem. C* 2011, **116**, 3305-3310.

60 Arunasish Layek, Suman De, Ruhi Thorat, Arindam Chowdhury, *J. Phys. Chem. Lett.*, 2011, ***2***, 1241–1247.

Figure Captions

Figure 1 (a-e) SEM images of ZnO nanoparticles synthesized using the sol-gel method followed by annealing in an ambient atmosphere at various temperatures. (f) Plot of distributions of the diameters of nanoparticles obtained from a portion of the SEM image of ZnO nanoparticles. The solid lines represent the fitting curves assuming the log-normal distribution function.

Figure 2 Growth temperature T_A dependence on the mean nanoparticle diameter $\langle d_{SEM} \rangle$, where the solid line shows the fit to the parabolic law and the fitted values are shown.

Figure 3 (a) Plot of EDS spectra taken from each ZnO nanoparticle. (b) The ratio of oxygen/zinc with respect to annealing temperature obtained by EDS.

Figure 4 Plots of the annealing temperature T_A dependence of the X-ray diffraction patterns taken at room temperature.

Figure 5 Linear fit obtained using the Williamson-Hall correlation for each ZnO nanoparticle where the slope of the graph gives the local lattice distortion and the intercept of the line to the y-axis gives the inverse particle size.

Figure 6 (a-e) The observed (crosses) and Rietveld refined (solid lines) X-ray patterns of ZnO nanoparticles synthesized at various annealing temperatures T_A. (f) Plot of the lattice constant with respect to nanoparticle size $\langle d_{XRD} \rangle$ obtained from the Williamson-Hall plot showing the increasing of R with decreasing particle size.

Figure 7 (a) Annealing temperature T_A dependence in Raman patterns taken at room temperature revealing a series of phonon modes E_{2H}-E_{2L}, E_{2H}, A_1(LO), TA+LO, A_1(2LO) and $2E_{1L}$ excitations. (b) The nanoparticle size $<d_{XRD}>$ dependence of the integrated intensity in the A_1(LO) and (c) ratio of the integrated intensity in the 2LO/LO, reflecting the weak- to strong-coupling strength of the electron-phonons with increasing particle size.

Figure 8 (a)-(b) The nanoparticle size $<d_{XRD}>$ dependence of the tensile- and compressive- strain. The solid lines represent the fitted results.

Figure 9 (a) Plot of the particle size dependency of the photoluminescence, where the solid line represents the superposition of the fit of two Gaussian functions. (b) Plot of the particle size dependency of the PL peak position obtained from the fit. (c) A schematic plot of the energy levels involved in the visible fluorescence.

Table 1 Summary of the fitting parameters obtained from the lognormal distribution function.

T_A(℃)	SEM analysis		
	$<d_{SEM}>$ (nm)	σ (nm)	χ^2
400	44±2	0.18±0.07	0.8263
500	60±5	0.19±0.02	0.9721
600	74±7	0.15±0.01	0.9776
700	115±14	0.09±0.01	0.8949
800	132±18	0.18±0.04	0.8549

Table 2 Summary of the fitting parameters obtained from the Rietveld refinement of the X-ray diffraction pattern.

T_A (℃)	$<d_{XRD}>$(nm)	FWHM (1 0 0) (rad.)	GSAS fitting parameters			Lattice constants		X	Y	Z	
			R_{wp}	R_p	χ^2	$a = b$ (Å)	c (Å)	Zn & O		Zn	O
400	32±1	0.0421±0.0001	0.0229	0.0120	1.646 0	3.2561±0.0003	5.2167±0.0005	1/3	2/3	0.004485	0.384485
500	38±2	0.0342±0.0004	0.0174	0.0107	0.8406	3.2549±0.0001	5.2148±0.0001	1/3	2/3	0.000380	0.375841
600	44±3	0.0302±0.0002	0.0152	0.0101	0.0152	3.2470±0.0001	5.2019±0.0001	1/3	2/3	0.002611	0.377389
700	51±2	0.0242±0.0002	0.0321	0.0189	1.7830	3.2467±0.0001	5.2013±0.0001	1/3	2/3	0.002758	0.377241
800	55±1	0.0193±0.0001	0.0288	0.0179	1.4480	3.2463±0.0001	5.2004±0.0001	1/3	2/3	0.000794	0.379206

Table 3 Summary of Voigt fitting parameters for Raman modes of ZnO nanoparticles.

T_A (℃)	$<d_{XRD}>$(nm)	$E_{2H} - E_{2L}$ (cm^{-1})		E_{2H} (cm^{-1})		A_1 (LO) (cm^{-1})		TA + LO (cm^{-1})		A_1 (2LO) (cm^{-1})		$2E_{1L}$ (cm^{-1})	
		Center	FWHM	Center	FWHM	Center	FWHM	Center	FWHM	Center	FWHM	Center	FWHM
400	32±1	330.0±0.7	26.73±1.4	437.5±0.2	15.82±1.6	583.1±0.7	25.20±2.6	658.5±6.9	107.60±8.9	1105.3	90.60	1153.6	40.78
500	38±2	329.8±0.6	27.36±1.9	437.5±0.1	15.49±1.8	582.6±0.6	26.40±2.9	658.4±3.9	39.49±2.5	1104.3	89.02	1154.1	43.80
600	44±3	329.7±0.6	26.40±2.0	437.4±0.1	14.92±0.9	581.8±0.4	27.89±1.9	662.2±4.1	67.38±3.8	1103.4	84.33	1153.7	46.20
700	51±2	329.7±0.7	10.09±0.9	437.3±0.2	14.12±1.1	581.1±0.7	34.90±3.5	658.6±6.9	79.74±4.5	1106.4	82.14	1155.4	42.70
800	55±1	329.5±0.5	23.68±1.7	436.8±0.3	11.93±0.8	580.8±1.4	37.70±3.1	659.6±3.6	81.18±7.8	1110.2	92.21	1156.1	40.88

Table 4 Summary of the Gaussian fitting parameters for the photoluminescence profiles of ZnO nanoparticles.

T_A (℃)	$<d_{XRD}>$ (nm)	PL first peak (nm)		PL second peak (nm)	
		Peak	FWHM	Peak	FWHM
400	32±1	569.6±0.4	84.48±1.42	628.4±4.3	140.90±4.26
500	38±2	674.2±5.2	138.15±0.38	768.2±2.4	156.91±2.02
600	44±3	685.2±13.1	149.78±5.23	788.9±45.0	150.96±1.98
700	51±2	699.8±2.0	200.36±2.60	846.1±6.5	59.74±9.21
800	55±1	725.7±1.6	199.54±1.98	852.6±5.2	43.47±7.26

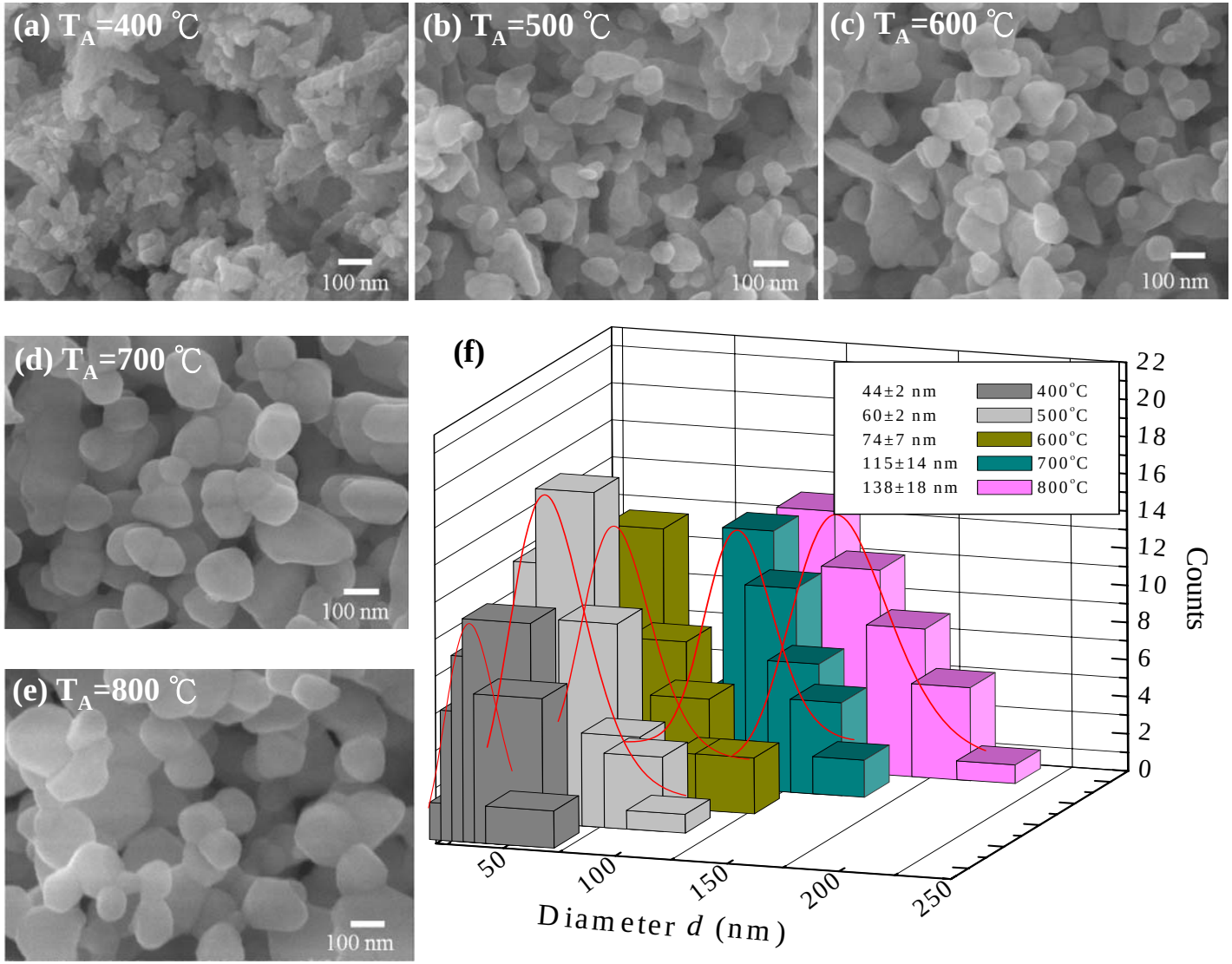

TC-ART-03-2014-000566 Figure 1

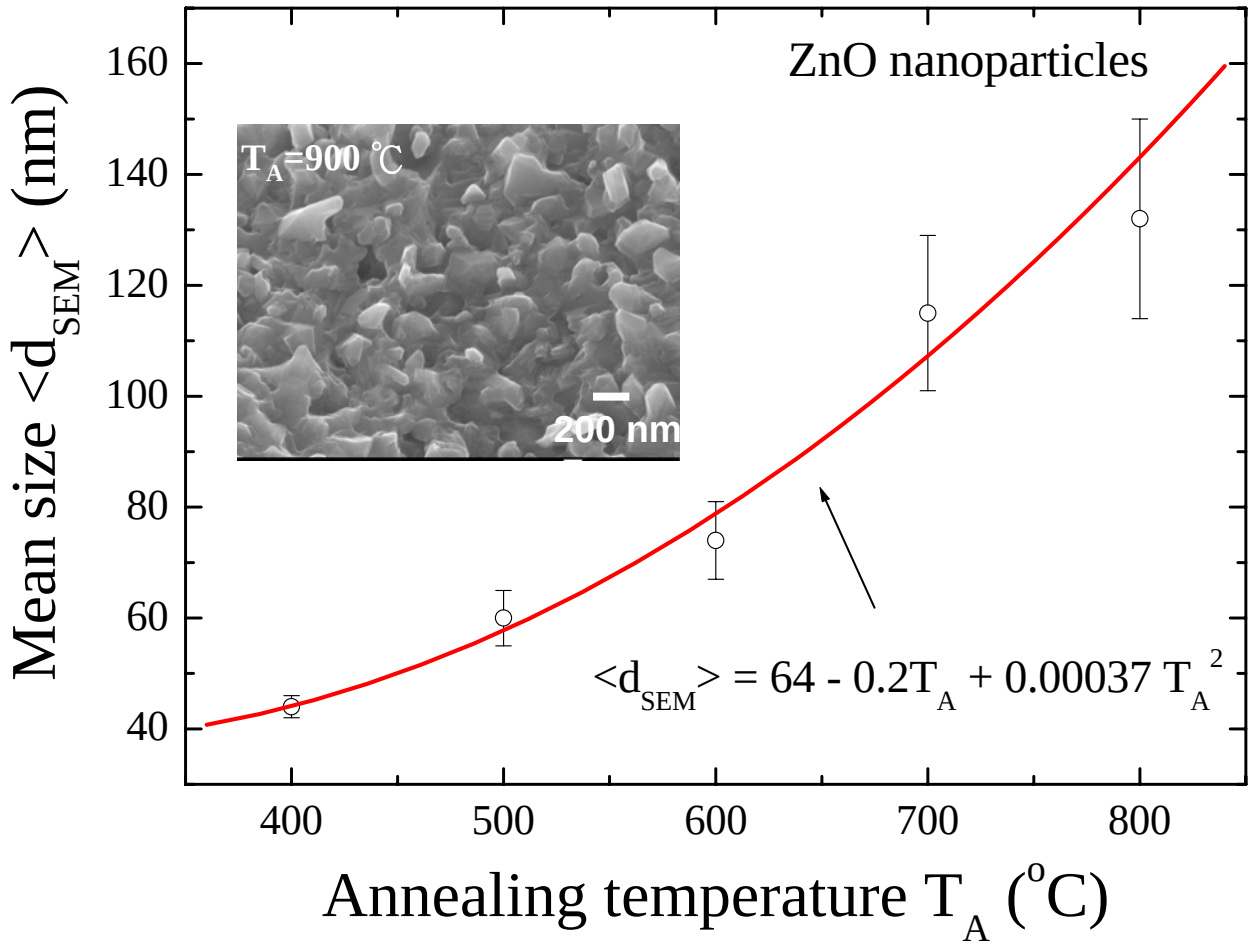

TC-ART-03-2014-000566 Figure 2

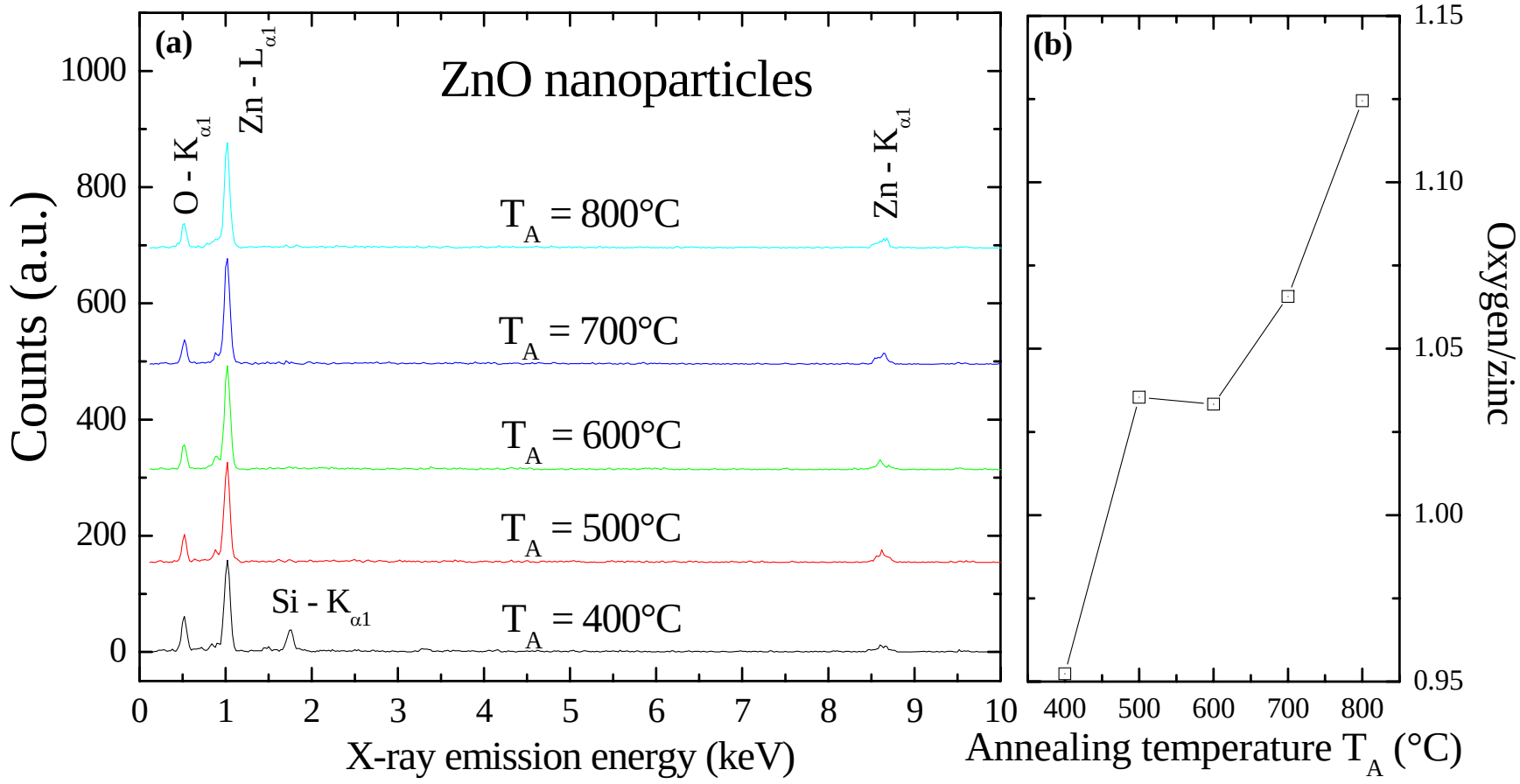

TC-ART-03-2014-000566 Figure 3

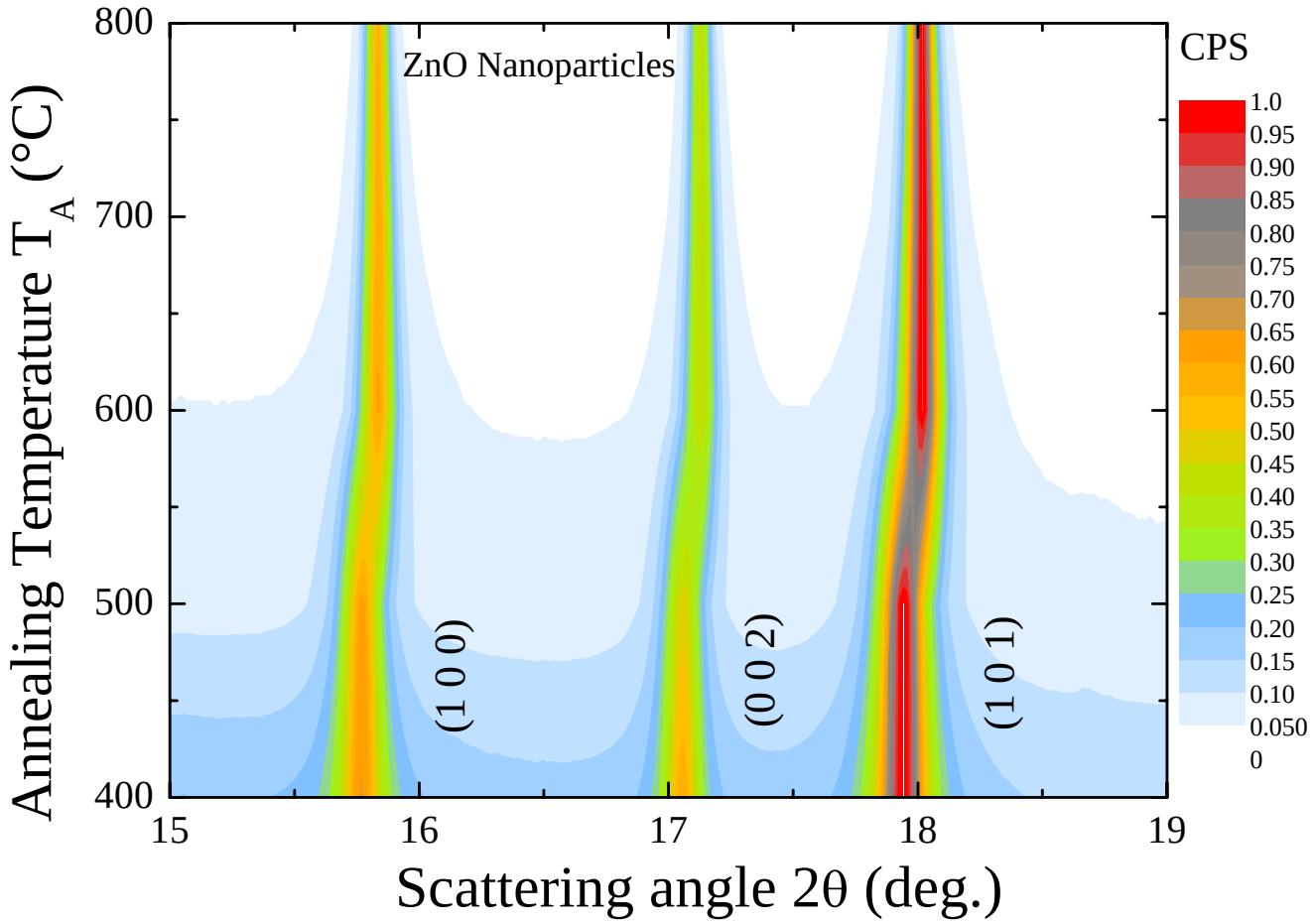

TC-ART-03-2014-000566 Figure 4

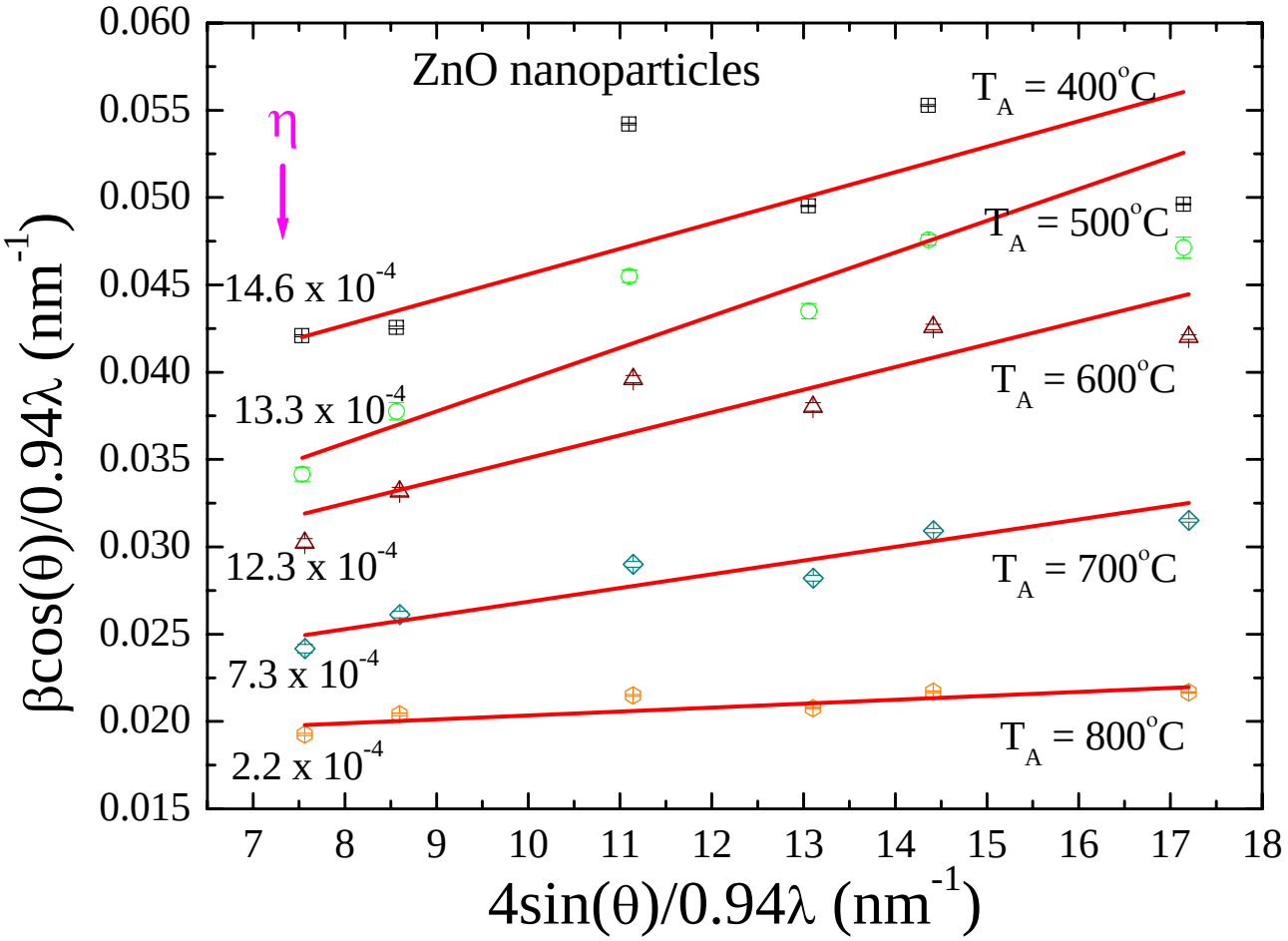

TC-ART-03-2014-000566 Figure 5

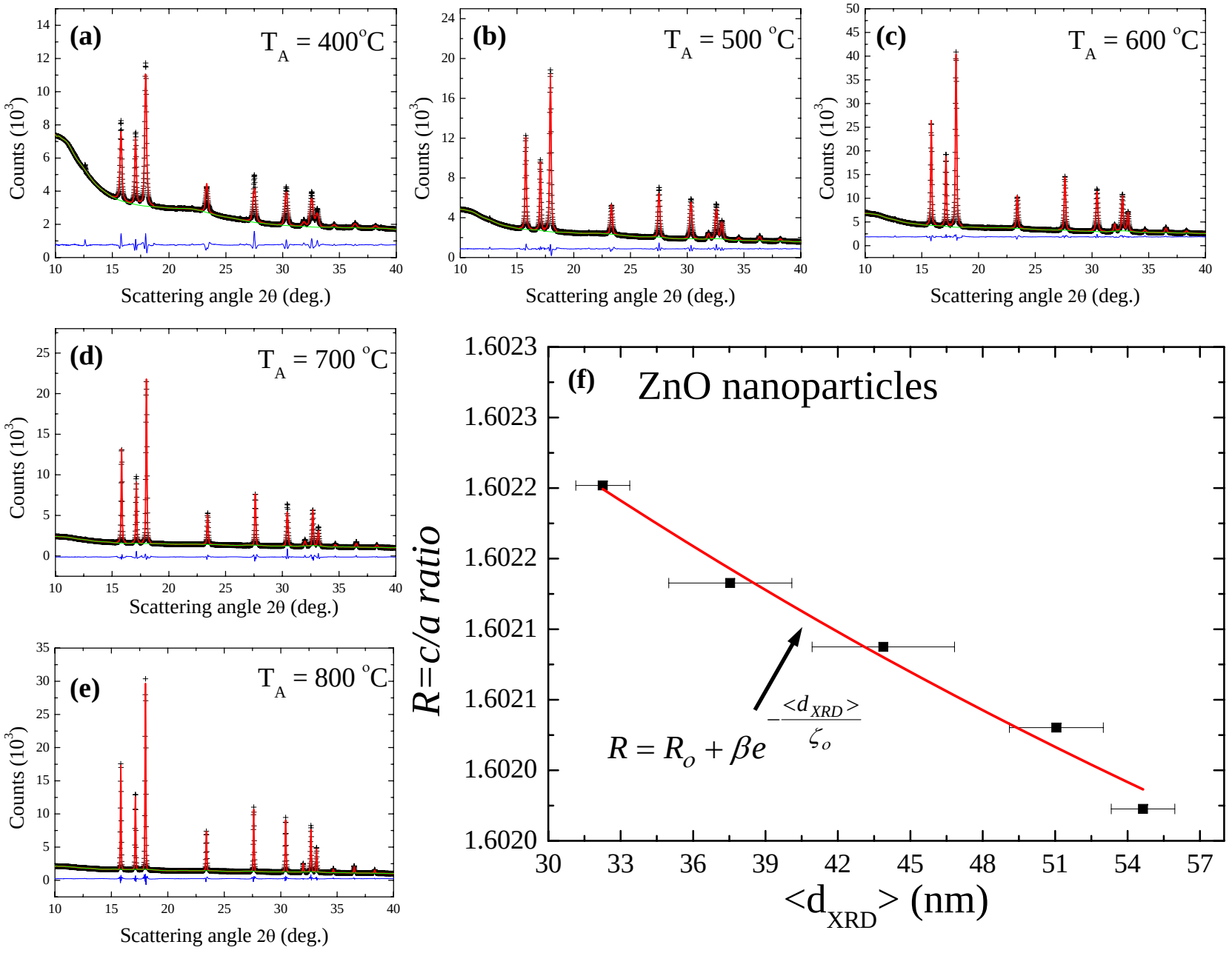

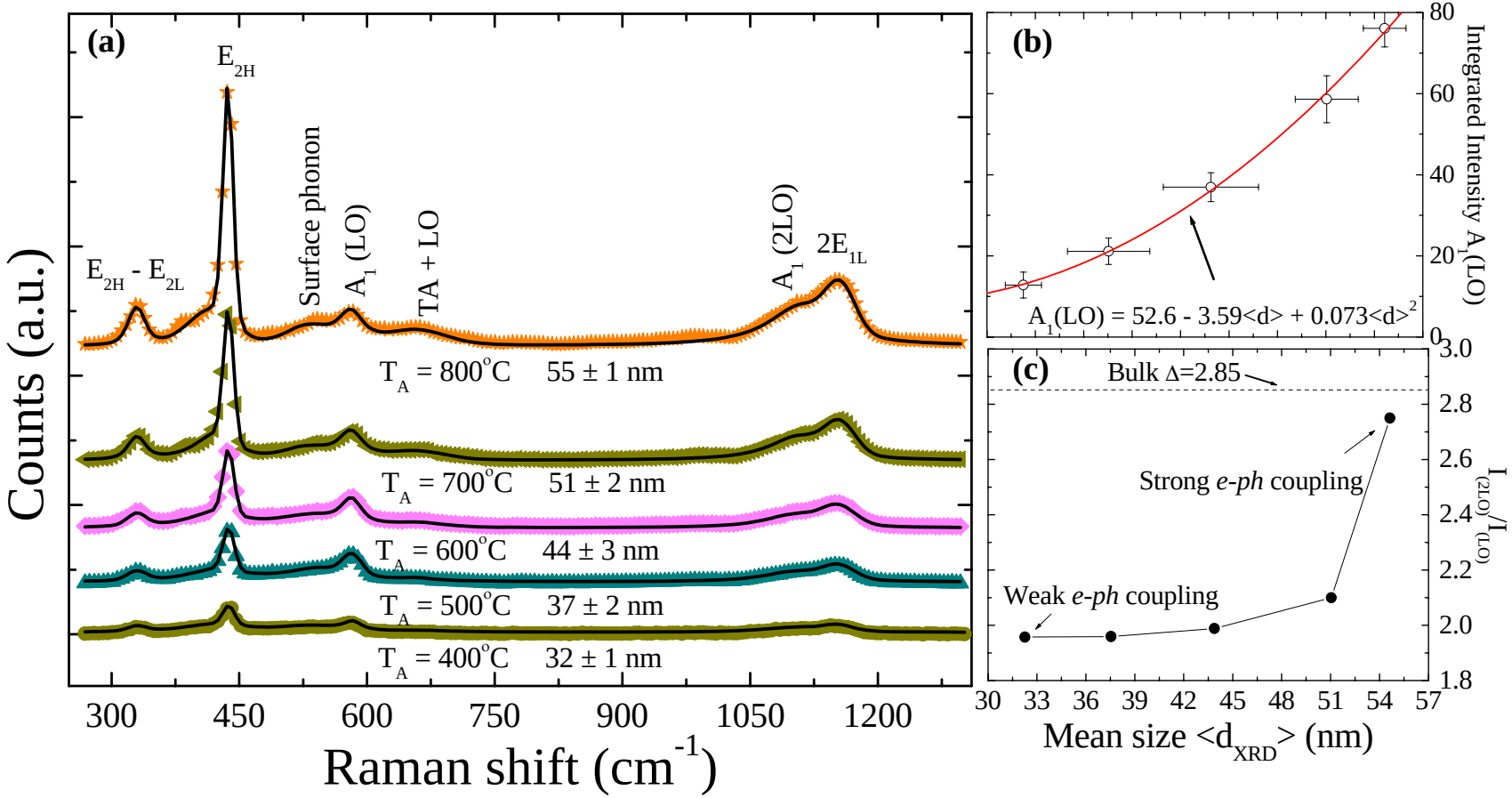

TC-ART-03-2014-000566 Figure 7

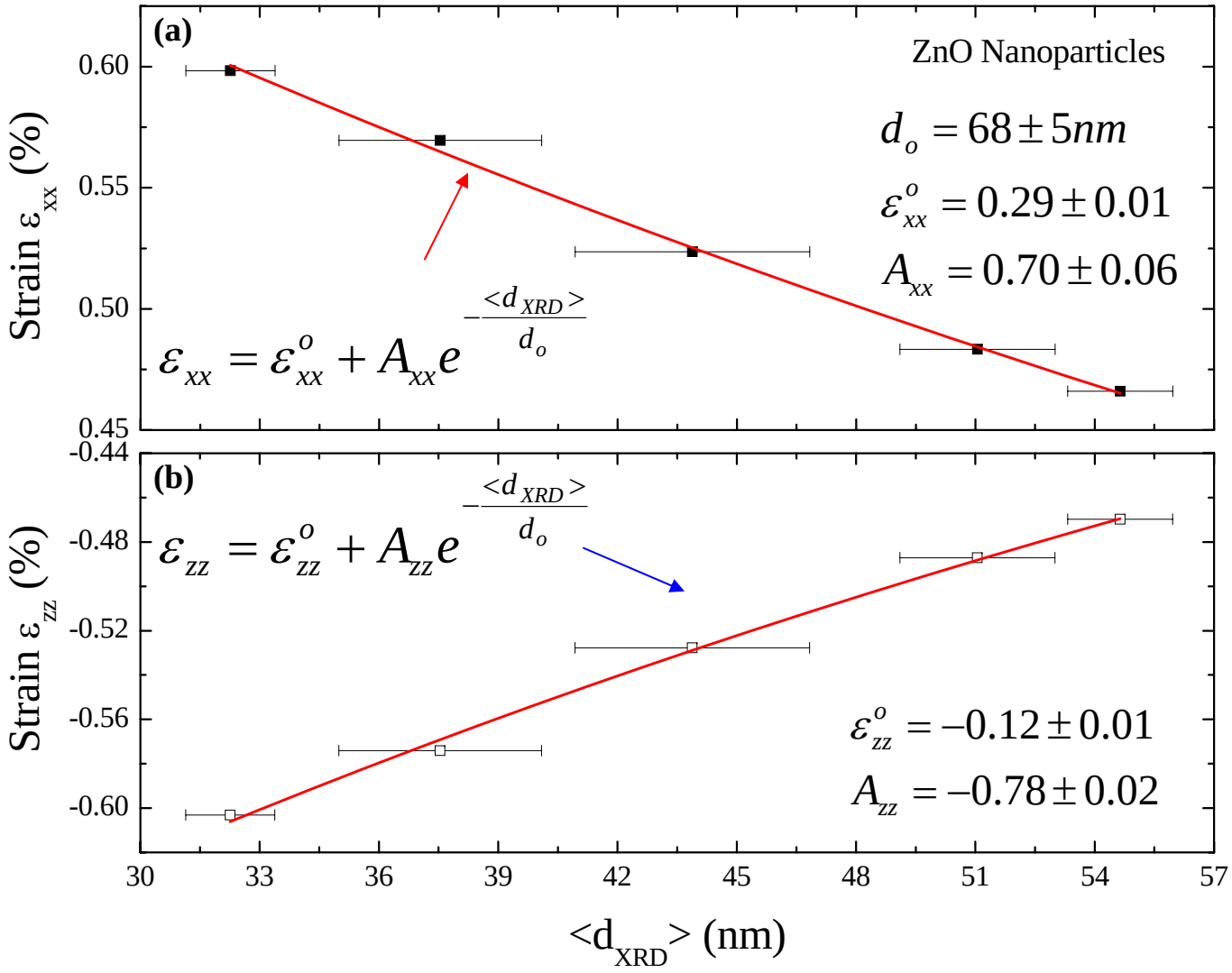

TC-ART-03-2014-000566 Figure 8

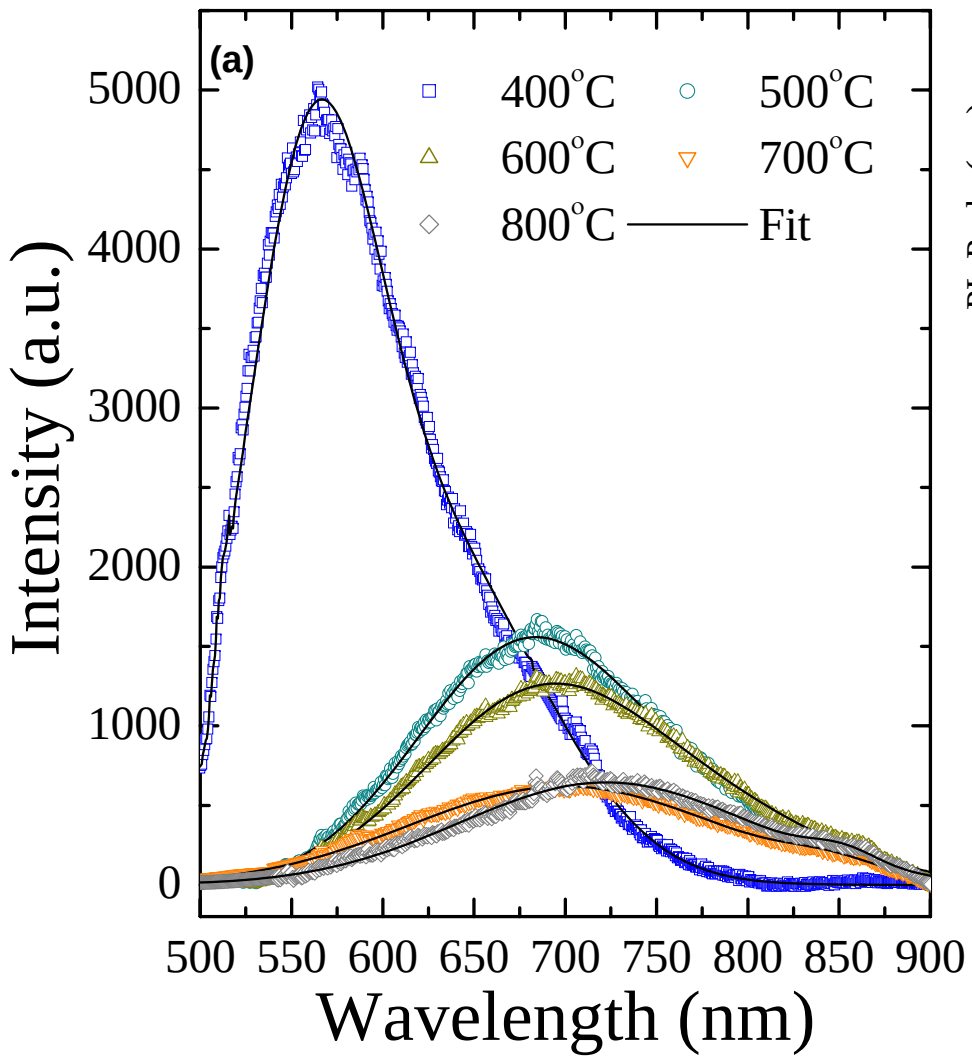

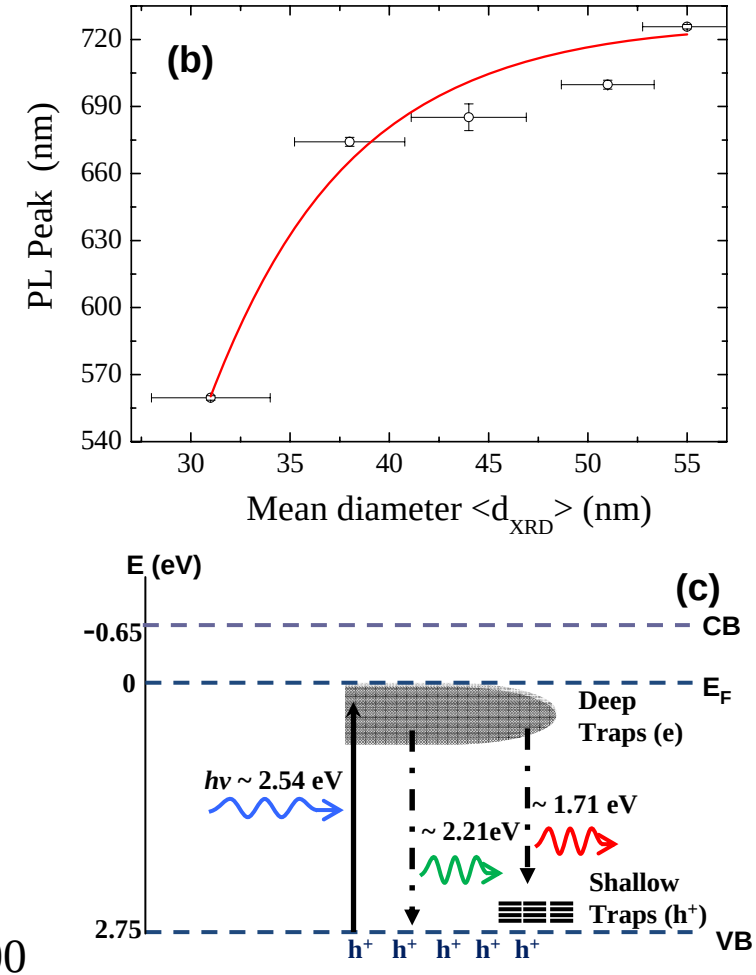

A schematic plot of the energy levels involved in the visible fluorescence.